博士研究生国家奖学金申请审批表

基本情况	姓名	张诚	性别	男	出生年月	1990 11
	政治面貌	党员	民族	汉	入学时间	2018 09
	学院	理学院	专业	物理学	学号	11849467
	学制	全日制	攻读学位	博士	学生类别	普通博士
	是否在 2021 年 9 月 30 日前完成开题且未完成预答辩：是☑ 否□					
	身份证号					

申请理由	尊敬的各位领导、老师： 本人热爱祖国，热爱集体，在思想上始终保持上进，拥护党和国家，遵纪守法。作为一名党员，在工作和学习上都严格要求自己，体现党员的先进性。紧跟时代热点，学习、贯彻和领会党的方针、政策和路线。认真履行作为一名博士研究生的职责，夯实本专业的知识、做好科学研究。在工作学习之余，我也积极参加学校或系里举办的各种学习和志愿者活动，例如学校篮球赛志愿者，图书馆志愿者等。在日常生活中，作为 2018 级博士的班长，我和同学们相处融洽，为同学们做些力所能及的服务。基于以上原因，我申请国家奖学金，希望能够借此来鞭策自己更加努力，成为更好的自己。 申请人签名：张诚 2021年 10 月 8 日

<table>
<tr><td>推荐
意见</td><td colspan="2">同意！
推荐人（导师）签名：黄丽
2020年10月8日</td></tr>
<tr><td>审核
意见</td><td>学生所在党支部意见：
支部书记签名：
年　　月　　日</td><td>基层党委意见：
党委书记签名（公章）：
年　　月　　日</td></tr>
<tr><td>评审
情况</td><td colspan="2">经评审，并在本单位内公示＿5＿个工作日，无异议，推荐该同学获得研究生国家奖学金。
评审委员会主任委员签名：
年　　月　　日</td></tr>
<tr><td>基层单位意见</td><td colspan="2">经评审，并在本单位内公示＿5＿个工作日，无异议，本单位申报该同学获得研究生国家奖学金。现报请研究生国家奖学金评审领导小组审定。
基层单位主管领导签名：
（基层单位公章）
年　　月　　日</td></tr>
<tr><td>培养单位意见</td><td colspan="2">经审核，并在本单位公示＿＿＿个工作日，无异议，现批准该同学获得研究生国家奖学金。
（培养单位公章）
年　　月　　日</td></tr>
</table>

南方科技大学 | 研究生院
SOUTHERN UNIVERSITY OF SCIENCE AND TECHNOLOGY
SUSTech Graduate School

南方科技大学

博士研究生成绩单

姓名	张诚	性别	男	出生日期	1990/11/03	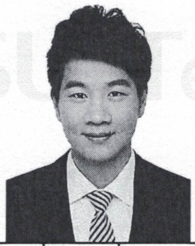
学号	11849467			入学时间	2018/09/03	
物理系		培养单位		物理学	学科	

课程代码	课程名称	学时	学分	考核方式	成绩	绩点	备注
GGC5003	科技论文检索与写作	32	2	考试	96	4	
GGC5016	博士英语	32	2	考试	91	4	
GGC5021	中国马克思主义与当代	32	2	考查	85	3.7	
PHY5005	物理实验仪器原理和应用	64	4	其它	94	4	
PHY5011	物理学中的群论	64	4	考查	85	3.7	
PHY5031	微纳结构加工	48	2	其它	89	3.7	
PHY5019	半导体器件物理	64	4	考查	80	3	
PHY5029	固体光电子学	48	3	考查	97	4	
ACA6011	论文开题考核		2	考查	通过		
ACA6012	博士资格考核		2	考查	通过		

完成课程学分/完成总学分　23/27　　学分

平均绩点　3.72

备注
1. GGC开头课程为公共课、ACA开头为必修培养环节，其余为专业课。
2. 该生为哈尔滨工业大学与南方科技大学联合培养，课程学习和必修环节在南方科技大学完成。

填表人　李爱晨

负责人：赵丹丹
南方科技大学研究生院(公章)
2021年10月07日

Applied Surface Science 570 (2021) 151178

Contents lists available at ScienceDirect

Applied Surface Science

journal homepage: www.elsevier.com/locate/apsusc

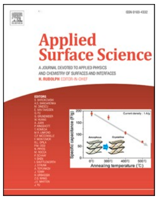

Full Length Article

Synthesis of ultrathin $PdSe_2$ flakes for hydrogen evolution reaction

Shaolong Jiang [a,1,*], Cheng Zhang [a,b,c,1], Erding Zhao [a], Mengjiao Han [a], Liang Zhu [a], Yu-Qing Zhao [d,*]

[a] *Department of Physics, Southern University of Science and Technology, Shenzhen 518055, China*
[b] *School of Physics, Harbin Institute of Technology, Harbin 150001, China*
[c] *Shenzhen Institute for Quantum Science and Engineering, Southern University of Science and Technology, Shenzhen 518055, China*
[d] *School of Physics and Electronics Science, Hunan University of Science and Technology, Xiangtan 411201, China*

ARTICLE INFO

Keywords:
2D materials
$PdSe_2$
Chemical vapor deposition
Hydrogen evolution reaction

ABSTRACT

Two-dimensional (2D) palladium diselenide ($PdSe_2$) has demonstrated great promise in electronics and optoelectronics due to its remarkable air stability, appealing carrier mobility, and controllable bandgap. However, realizing the synthesis of 2D $PdSe_2$ remains still a daunting challenge. Herein, high-quality, ultrathin (~2.2 nm) 2D $PdSe_2$ flakes are achieved on mica substrates through a NaCl-assisted ambient-pressure chemical vapor deposition method. We systematically probe the crystal quality and optical characteristics in $PdSe_2$ using scanning transmission electron microscopy, angle-resolved polarized Raman spectroscopy, and second harmonic generation characterizations. Impressively, the transferred $PdSe_2$ flakes on Au foil, featuring lower overpotential of ~ 150 mV at 10 mA/cm^2, lower Tafel slope of ~ 70 mV/dec, higher exchange current density of ~ 85 μA/cm^2, and superior stability, display outstanding electrocatalytic performance for hydrogen evolution reaction (HER). This work shows a promising prospect of $PdSe_2$ in electrocatalysis for HER.

1. Introduction

Two-dimensional (2D) transition metal dichalcogenides (TMDCs) are fundamentally important for developing next-generation electronics [1,2], optoelectronics [3,4], electrocatalysis [5,6], and so on, due to their unique physical properties. Among them, especially palladium diselenide ($PdSe_2$), as a puckered pentagonal material, possesses robust carrier mobility, highly tunable bandgap ranging from 0 eV (bulk) to 1.3 eV (monolayer), as well as prominent air stability [7–9]. Furthermore, $PdSe_2$ demonstrates a variety of peculiar properties resulting in various applications ranging from field-effect transistors [7,8,10], photodetectors [11–15], and electrocatalysts for hydrogen evolution reaction (HER) [16,17] to thermoelectrics [18] and memristors [19]. However, the synthesis of high-quality, ultrathin 2D $PdSe_2$ still remain challenging, tremendously hindering its practical applications. Up to now, mechanically exfoliated $PdSe_2$ suffers from the uncontrollable thickness and geometry [7,8,20]. Recently, the preparation of high-quality 2D $PdSe_2$ by chemical vapor deposition (CVD) methods has been realized but rare [21–25]. Additionally, given that 2D noble-TMDCs such as $PtTe_2$ and $PtSe_2$ have excellent catalytic property for HER [26–28], as well as few-layer semiconducting $PdSe_2$ possesses zero-gap edges due to the hybridization of Pd 4d and Se 4p orbitals [9], there is expectation that the outstanding electrocatalytic HER performance would occur for 2D $PdSe_2$, which needs experimental certification. Hence, it is urgent to find effective solutions to resolve aforementioned issues.

Herein, high-quality, ultrathin 2D $PdSe_2$ flakes have been successfully synthesized on mica substrates via a NaCl-assisted ambient-pressure CVD (APCVD) technique. The element uniformity, crystalline quality, and optical features of rectangular $PdSe_2$ flakes as thin as ~ 2.2 nm are intensively investigated by energy-dispersive X-ray spectroscopy (EDS), transmission electron microscopy (TEM), scanning transmission electron microscopy (STEM), Raman spectroscopy, and second harmonic generation (SHG) techniques. Meaningfully, the CVD-derived $PdSe_2$ flakes transferred onto Au foils, as working electrodes, demonstrate a fantastic nature with low overpotential, small Tafel slope, large exchange current density, and excellent durability for electrocatalytic HER. Our study enables a facile synthesis method for fabricating high-quality, ultrathin 2D $PdSe_2$ flakes with good HER catalytic activities.

---

* Corresponding authors.
E-mail addresses: jiangsl@sustech.edu.cn (S. Jiang), yqzhao@hnu.edu.cn (Y.-Q. Zhao).

[1] Shaolong Jiang and Cheng Zhang contributed equally to this work.

https://doi.org/10.1016/j.apsusc.2021.151178
Received 27 June 2021; Received in revised form 18 August 2021; Accepted 1 September 2021

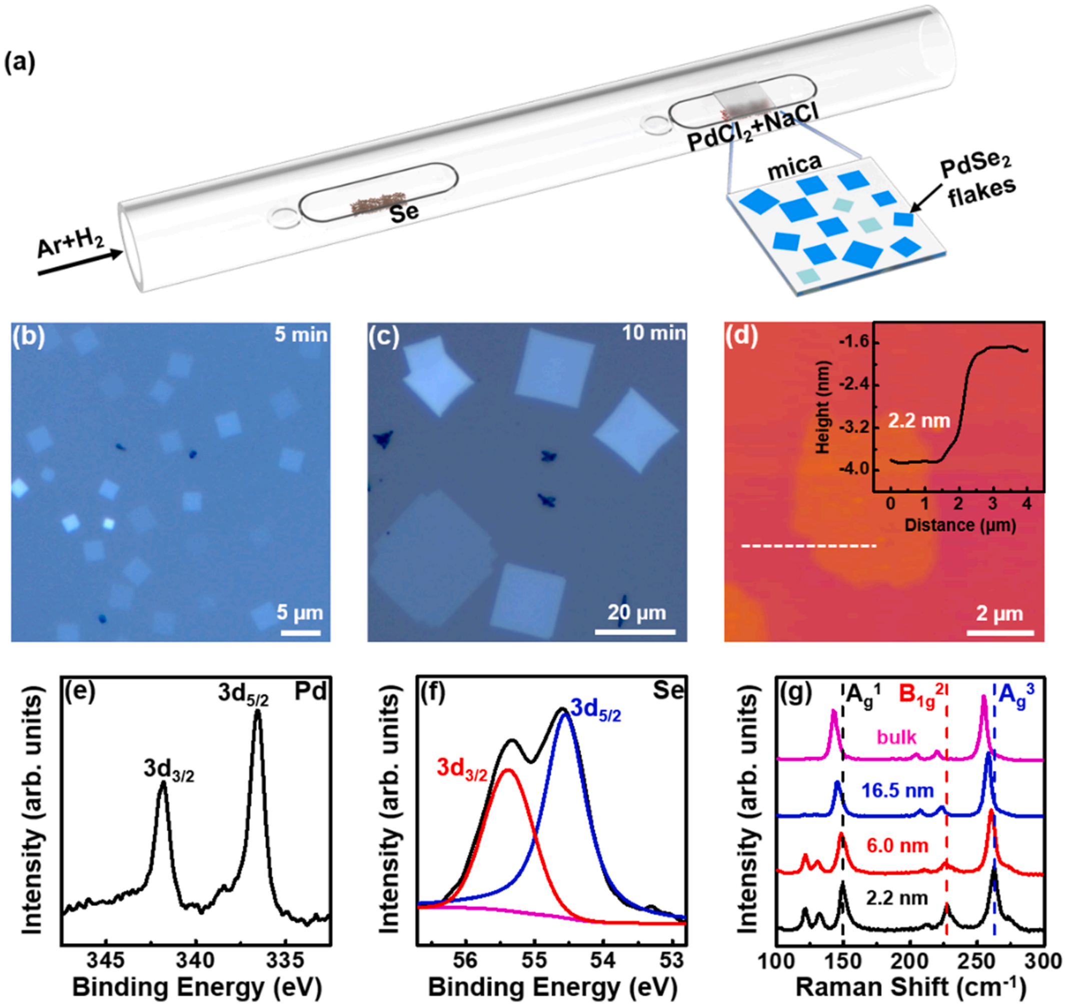

Fig. 1. Synthesis of ultrathin 2D $PdSe_2$ flakes. (a) Schematic diagram of preparing ultrathin 2D $PdSe_2$ flakes on mica substrates by APCVD. (b, c) OM images of as-grown $PdSe_2$ flakes on mica with growth time of 5 and 10 min, respectively. (d) AFM image and the height profile of a $PdSe_2$ flake on mica. (e, f) XPS spectra of Pd 3d (e) and Se 3d (f). (g) Thickness dependence of Raman spectra for $PdSe_2$ flakes.

2. Experimental section

2.1. Preparation of $PdSe_2$

2D $PdSe_2$ single-crystal flakes were synthesized via an APCVD technique. Powders of Se (0.3 g, 99+%, Alfa Aesar) and $PdCl_2$/NaCl (10 mg, 99.999%, Alfa Aesar; 1 mg, 99.999%, Alfa Aesar) were used as sources. Se powder (350 °C) was put upstream and $PdCl_2$/NaCl powders (850 °C) were placed in the center of the furnace with mica put above them as growth substrate. Before heating, high purity Ar (300 sccm) was utilized to purge the tube furnace for 15 min. Ar (80 sccm) and H_2 (15 sccm) were used as carrier gases. After 5–10 min growth, the furnace was naturally cooled down to room temperature. Then, the fabricated $PdSe_2$ flakes on mica were transferred onto target substrates via a poly (methyl methacrylate)-mediated method.

2.2. Characterization of $PdSe_2$

$PdSe_2$ flakes were characterized by OM (Zeiss Axioscope 5), AFM (Asylum Research Cypher S), XPS (PHI 5000 Versaprobe III with monochromatic Al Kα X-ray, ULVAC-PHI), Raman spectroscopy (HORIBA XploRA PLUS and HORIBA iHR550, 532 nm laser), SHG (HORIBA iHR320, 800 nm laser), SEM (Phenom LE, 15 kV) equipped with an EDS, TEM (FEI Tecnai F30, acceleration voltage of 300 kV), and STEM (JEOL JEM-ARM200CF, acceleration voltage of 200 kV).

2.3. Electrochemical measurements

Electrochemical measurements were carried out in a three-electrode system at an electrochemical workstation (CHI 660D), with the transferred $PdSe_2$ flakes on Au foil as the working electrode, a saturated calomel reference electrode, and a Pt foil as the counter electrode, respectively. All the potentials were calibrated to a reversible hydrogen electrode (RHE). Linear sweep voltammetry was conducted in 99.999 % N_2-saturated 0.5 M H_2SO_4 electrolyte with a scan rate of 5 mV/s.

3. Results and discussion

Ultrathin 2D $PdSe_2$ crystals were directly synthesized by a NaCl-assisted APCVD method (Fig. 1a). Se powder placed upstream and $PdCl_2$/NaCl powders placed at the center of the furnace were utilized as selenium and palladium sources, respectively. Mica placed on $PdCl_2$/NaCl powders was utilized as growth substrates. The $PdSe_2$ flakes grew on mica at growth temperature of 850 °C with mixed carrier gases of H_2 and Ar. More sample growth details are depicted in the Experimental section. The crystal structure model of 2D $PdSe_2$ is described in Fig. S1 in the Supporting Information. Optical microscopy (OM) images display that the achieved $PdSe_2$ flakes show a rectangular morphology due to its orthorhombic structure, with the maximum lateral size from ~ 3 (growth time of 5 min) to ~ 28 μm (growth time of 10 min) (Fig. 1b and 1c). As shown in Fig. 1d and S2 in the Supporting Information, atomic

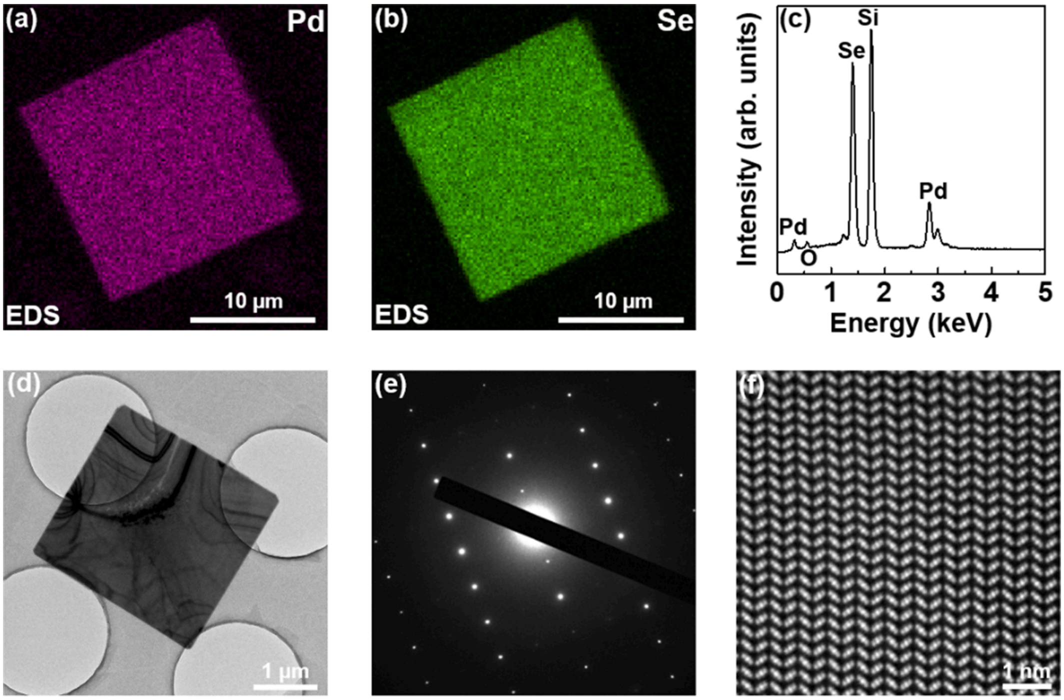

Fig. 2. EDS, TEM, and STEM characteristics of $PdSe_2$ flakes. (a, b) EDS elemental mappings of Pd (a) and Se (b) of a $PdSe_2$ flake transferred onto SiO_2/Si. (c) EDS spectrum of the transferred $PdSe_2$ flake on SiO_2/Si. (d-f) Low-magnification TEM image (d), the corresponding SAED pattern (e), and HAADF-STEM image (f) of the $PdSe_2$ flake.

force microscopy (AFM) images depict that the CVD-$PdSe_2$ flakes possess a thinnest thickness down to ~ 2.2 nm. In addition, X-ray photoelectron spectroscopy (XPS) was carried out to identify the chemical states of the prepared $PdSe_2$ flakes (Fig. 1e and 1f). The chemical states of element Pd ($3d_{3/2}$: ~341.9 eV; $3d_{5/2}$: ~336.6 eV) are related to Pd^{4+}, and the chemical states of element Se ($3d_{3/2}$: ~55.4 eV; $3d_{5/2}$: ~54.5 eV) are assigned to Se^{2-}. The phonon vibrations and interlayer coupling of as-fabricated $PdSe_2$ flakes were characterized using Raman spectroscopy. As demonstrated in Fig. 1g, the Raman peaks located at ~ 143.1, ~219.9, and ~ 255.1 cm^{-1} are ascribed to the A_g^1, B_{1g}^2, and A_g^3 vibrational modes of bulk $PdSe_2$, respectively. With decreasing thickness to 2.2 nm, the three vibrational modes show the striking blueshift to ~ 149.5 (A_g^1), ~227.5 (B_{1g}^2), and ~ 262.7 (A_g^3) cm^{-1}, respectively, due to the strong interlayer coupling and hybridization in $PdSe_2$ [7]. Briefly, ultrathin 2D $PdSe_2$ flakes can be successfully fabricated on mica using a NaCl- aided APCVD method.

The EDS characterization was then carried out to explore the elemental composition and distribution of the CVD-derived $PdSe_2$ flakes. EDS elemental mappings are displayed in Fig. 2a and 2b, demonstrating the uniformity of elements Pd and Se distribution across the whole $PdSe_2$ flake transferred onto SiO_2/Si (Fig. S3 in the Supporting Information). In addition, EDS spectrum (Fig. 2c) shows sharp Pd and Se element peaks with an atomic ratio of ~ 1:1.99, revealing that our CVD-grown sample is stoichiometric $PdSe_2$. The TEM and STEM were used for further demonstrating the crystallinity and crystal structure of the CVD-synthesized $PdSe_2$ flakes. The low-magnification TEM image of a $PdSe_2$ flake transferred onto a Cu grid is displayed in Fig. 2d. The selected area electron diffraction (SAED) pattern (Fig. 2e) reveals that the as-grown $PdSe_2$ flakes agree well with great crystallinity and are single crystals. As exhibited in Fig. 2f, the atomic-resolution high-angle annular dark-field (HAADF) STEM image of the $PdSe_2$ indicates the orthorhombic lattice without evident crystal defects. Therefore, high-quality, ultrathin 2D $PdSe_2$ single crystals can be prepared on mica by APCVD.

Angle-resolved polarized Raman spectroscopy (ARPRS) was conducted to probe the crystal orientation and phonon vibrational anisotropy of the CVD-derived $PdSe_2$ under a parallel polarization configuration. The OM image of the $PdSe_2$ flake transferred onto SiO_2/Si for ARPRS measurement is presented in Fig. 3a. Fig. 3b depicts the polarization-dependent Raman spectra obtained every 10° from 0° to 180° by the rotation of $PdSe_2$ sample, revealing obvious variation of the intensity of each peak with the sample rotation angle. For instance, the A_g^1 mode exhibits the maximum at 0° and 180°, corresponding to the direction along the *a* axis [23], and the B_{1g}^2 mode reaches the maximum at 40° and 130° (Fig. 3c). Briefly, ARPRS measurement can recognize the crystal orientation of our CVD-grown $PdSe_2$ sample.

The nonlinear optical properties of 2D TMDCs materials have been widely investigated using SHG microscopy. Particularly, even-layered $PdSe_2$, which pertains to the $Pca2_1$ (No. 29) space group, could present a striking SHG response because of the absence of inversion symmetry [29]. The SHG signals on our CVD-derived 2D $PdSe_2$ flake were performed to probe its nonlinear properties under a 800 nm excitation laser. Fig. 4a illustrates the schematic diagram of SHG measurement for the $PdSe_2$ flake. Angle-resolved polarized SHG characterization was carried out to further study the optical anisotropy of 2D $PdSe_2$ under parallel configuration, demonstrating that the SHG intensity has a distinct two-petal pattern (Fig. 4b), which agrees well with the structure symmetry of pentagonal $PdSe_2$. The power-dependent SHG spectra of 2D $PdSe_2$ flake are displayed in Fig. 4c, revealing that the SHG intensity exhibits remarkable enhancement with increasing the excitation power from 0.6 to 1.0 mW. In addition, the SHG signals are observed at ~ 400 nm. Moreover, the linear fitting in logarithmic coordinates is obtained for the power-dependent SHG intensity, which shows a slope of ~2.07 approaching the theoretical value 2, as demonstrated in Fig. 4d,

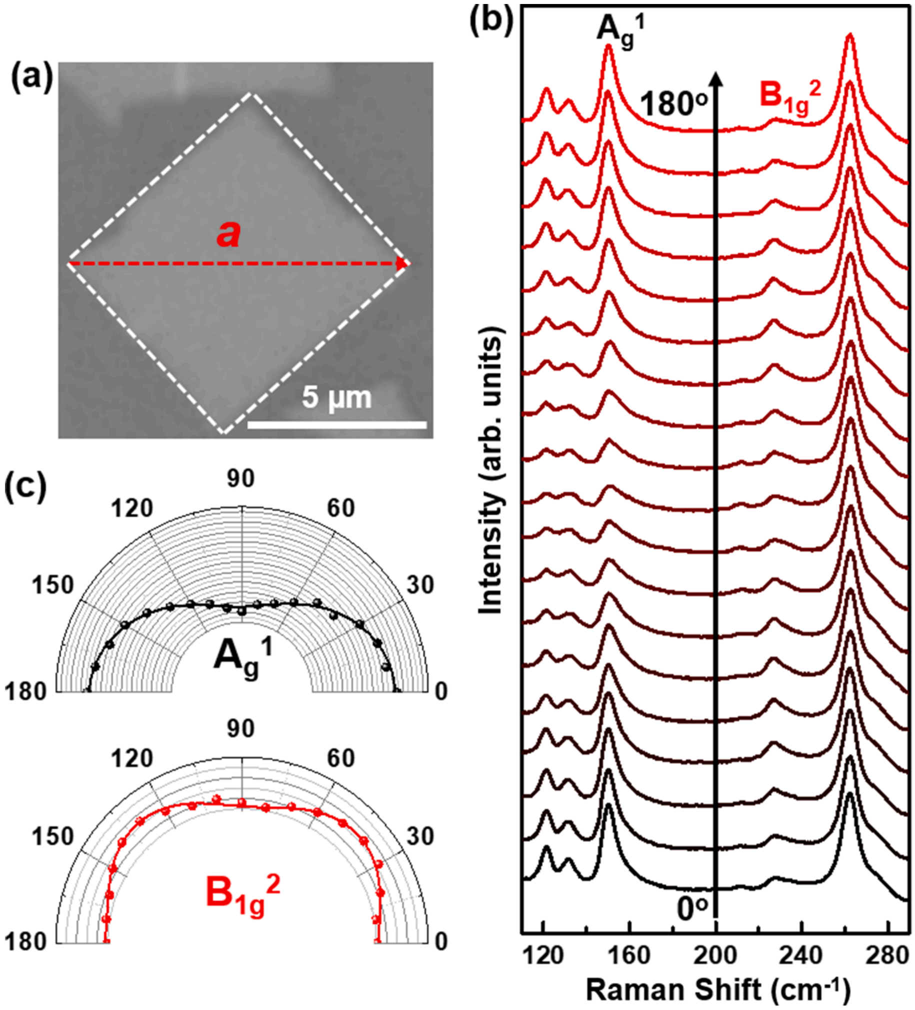

Fig. 3. Angle-resolved Raman characterization of the $PdSe_2$ flake. (a) OM image of the transferred $PdSe_2$ flake on SiO_2/Si. (b) Angle-resolved polarized Raman spectra of the $PdSe_2$ flake. (c) Polar plots of Raman intensity of $A_g{}^1$ and $B_{1g}{}^2$.

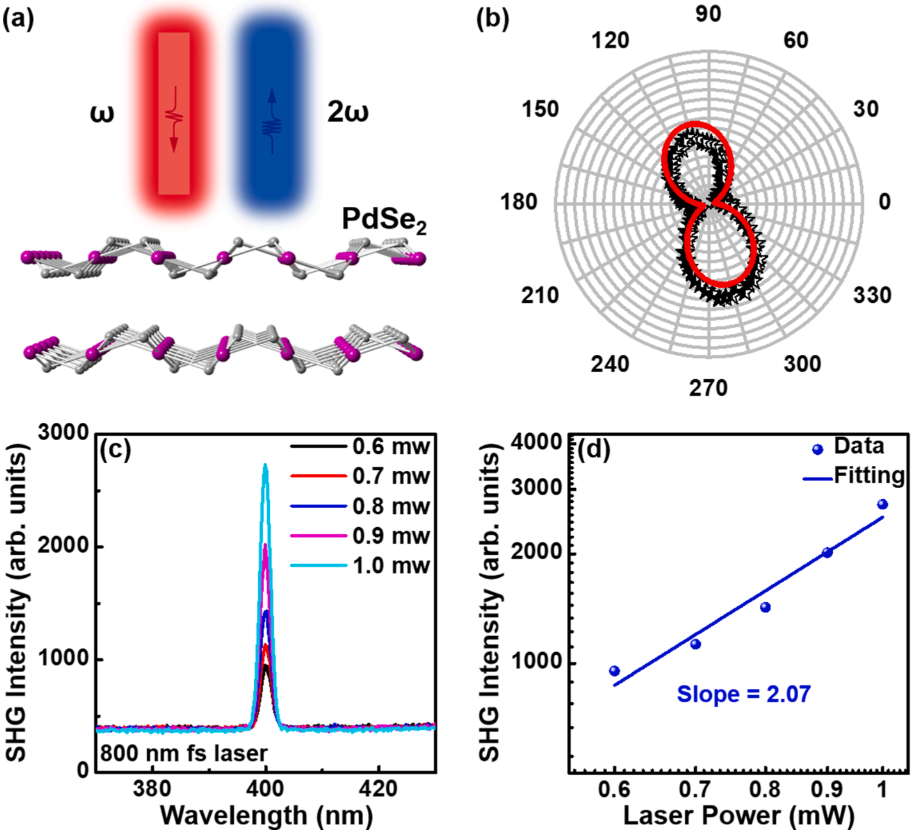

Fig. 4. SHG characterization of 2D PdSe$_2$ flake under excitation wavelength of 800 nm. (a) Schematic diagram of the measurement of SHG for the PdSe$_2$ flake. (b) Polarization-resolved SHG of 2D PdSe$_2$ under parallel configuration. (c) Power-dependent SHG response of 2D PdSe$_2$. (d) Power-dependent SHG intensity for the PdSe$_2$ flake in logarithmic coordinates.

consistent with the feature of second-order nonlinear process [30].

The electrocatalytic performance of the PdSe$_2$ flakes was then assessed in 0.5 M H_2SO_4 electrolyte. Considering the poor conductivity of mica, the as-synthesized PdSe$_2$ flakes were transferred onto Au foil ahead of the measurements of HER. Fig. S4 in the Supporting Information shows the transferred PdSe$_2$ electrocatalysts on Au foil (grown for 5 min). The polarization curve depicts the HER activity of the transferred PdSe$_2$ sample (Fig. 5a), with that for Au foil as a reference. It is worth emphasizing that the PdSe$_2$/Au electrode has much lower onset overpotential than the pure Au electrode, revealing the markedly improved HER activity of PdSe$_2$ and showing an overpotential of ~ 150 mV at a current density of 10 mA/cm^2. Tafel analysis displays that the linear region possesses the slope of ~ 70 mV/dec for PdSe$_2$ sample (Fig. 5b), further manifesting the excellent HER catalytic activity. In addition, the exchange current density was obtained using the Tafel plot extrapolation method for the PdSe$_2$ product (Fig. 5c), where it shows the value of ~ 85 μA/cm^2, suggestive of its high activity in HER. Lastly, the long-term stability was evaluated for the transferred PdSe$_2$ product in Fig. 5d, demonstrating minor decay of catalytic property after 1000 electrochemical cycles, revealing that this material is a promising electrocatalyst for HER.

4. Conclusions

In conclusion, we have successfully fabricated high-quality, ultrathin 2D PdSe$_2$ flakes thin to ~ 2.2 nm on mica via a NaCl-assisted APCVD method. The crystalline quality and optical properties are investigated by HAADF-STEM, ARPRS, and SHG characterizations. Significantly, the PdSe$_2$ flakes transferred onto Au foil show superior HER catalytic activity, featuring low overpotential of ~ 150 mV at 10 mA/cm^2, small Tafel slope of ~ 70 mV/dec, large exchange current density of ~ 85 μA/cm^2, and good durability. We believe that 2D PdSe$_2$ is prospective for applications in HER electrocatalysis.

CRediT authorship contribution statement

Shaolong Jiang: Data curation, Formal analysis, Investigation, Methodology, Project administration, Supervision, Writing - original draft, Writing - review & editing. **Cheng Zhang:** Data curation, Formal analysis. **Erding Zhao:** Data curation, Formal analysis. **Mengjiao Han:** Data curation, Formal analysis. **Liang Zhu:** Data curation, Formal analysis. **Yu-Qing Zhao:** Data curation, Formal analysis, Funding acquisition, Writing - original draft, Writing - review & editing.

Declaration of Competing Interest

The authors declare that they have no known competing financial interests or personal relationships that could have appeared to influence the work reported in this paper.

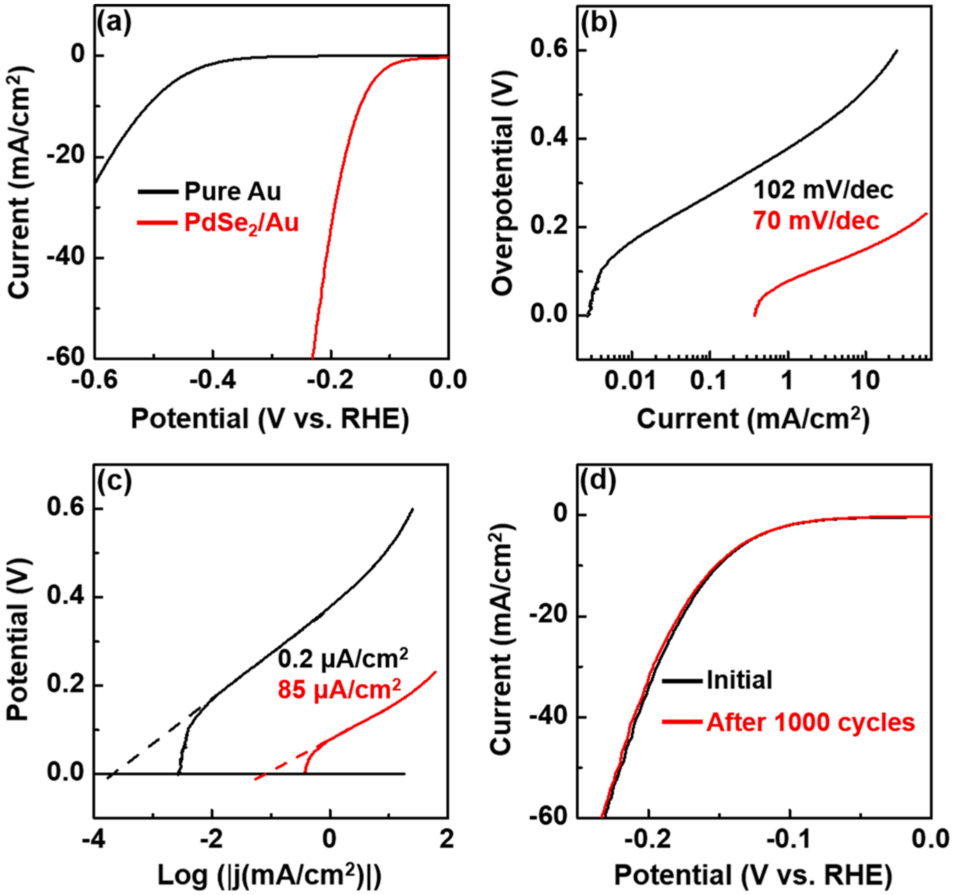

Fig. 5. HER performance of the $PdSe_2$ flakes transferred onto Au foil. (a) Polarization curve of the transferred $PdSe_2$ sample along with that of pure Au foil for comparison. (b, c) Corresponding Tafel plots and exchange current densities calculated based on Tafel plot extrapolation method, respectively. (d) Durability test for the $PdSe_2$ flakes.

Acknowledgements

The work was supported by the Scientific Research Fund of Hunan Provincial Education Department, China (No. 20B219) and the Hunan Provincial Natural Science Foundation of China (No. 2020JJ5154).

Appendix A. Supplementary data

Supplementary data to this article can be found online at https://doi.org/10.1016/j.apsusc.2021.151178.

References

[1] M. Chhowalla, H.S. Shin, G. Eda, L.-J. Li, K.P. Loh, H. Zhang, The chemistry of two-dimensional layered transition metal dichalcogenide nanosheets, Nat. Chem. 5 (2013) 263–275.

[2] F. Cui, C. Wang, X. Li, G. Wang, K. Liu, Z. Yang, Q. Feng, X. Liang, Z. Zhang, S. Liu, Z. Lei, Z. Liu, H. Xu, J. Zhang, Tellurium-assisted epitaxial growth of large-area, highly crystalline ReS_2 atomic layers on mica substrate, Adv. Mater. 28 (2016) 5019–5024.

[3] T. Yang, B. Zheng, Z. Wang, T. Xu, C. Pan, J. Zou, X. Zhang, Z. Qi, H. Liu, Y. Feng, W. Hu, F. Miao, L. Sun, X. Duan, A. Pan, Van der Waals epitaxial growth and optoelectronics of large-scale WSe_2/SnS_2 vertical bilayer p-n junctions, Nat. Commun. 8 (2017) 1906.

[4] Y. Yang, K. Zhang, L. Zhang, G. Hong, C. Chen, H. Jing, J. Lu, P. Wang, X. Chen, L. Wang, H. Xu, Controllable growth of type-II Dirac semimetal $PtTe_2$ atomic layer on Au substrate for sensitive room temperature terahertz photodetection, InfoMat. 3 (2021) 705–715.

[5] Q. Zhang, L. Fu, Novel insights and perspectives into weakly coupled ReS_2 toward emerging applications, Chem. 5 (2019) 505–525.

[6] C. Zhang, Y. Luo, J. Tan, Q. Yu, F. Yang, Z. Zhang, L. Yang, H.-M. Cheng, B. Liu, High-throughput production of cheap mineral-based two-dimensional electrocatalysts for high-current-density hydrogen evolution, Nat. Commun. 11 (2020) 3724.

[7] A.D. Oyedele, S. Yang, L. Liang, A.A. Puretzky, K. Wang, J. Zhang, P. Yu, P. R. Pudasaini, A.W. Ghosh, Z. Liu, C.M. Rouleau, B.G. Sumpter, M.F. Chisholm, W. Zhou, P.D. Rack, D.B. Geohegan, K. Xiao, $PdSe_2$: Pentagonal two-dimensional layers with high air stability for electronics, J. Am. Chem. Soc. 139 (2017) 14090–14097.

[8] W.L. Chow, P. Yu, F. Liu, J. Hong, X. Wang, Q. Zeng, C.-H. Hsu, C. Zhu, J. Zhou, X. Wang, J. Xia, J. Yan, Y. Chen, D. Wu, T. Yu, Z. Shen, H. Lin, C. Jin, B.K. Tay, Z. Liu, High mobility 2D palladium diselenide field-effect transistors with tunable ambipolar characteristics, Adv. Mater. 29 (2017), 1602969.

[9] C. Xie, S. Jiang, Y. Gao, M. Hong, S. Pan, J. Zhao, Y. Zhang, Giant thickness-tunable bandgap and robust air stability of 2D palladium diselenide, Small 16 (2020), 2000754.

[10] A.D. Oyedele, S. Yang, T. Feng, A.V. Haglund, Y. Gu, A.A. Puretzky, D. Briggs, C. M. Rouleau, M.F. Chisholm, R.R. Unocic, D. Mandrus, H.M. Meyer, S.T. Pantelides, D.B. Geohegan, K. Xiao, Defect-mediated phase transformation in anisotropic two-dimensional $PdSe_2$ crystals for seamless electrical contacts, J. Am. Chem. Soc. 141 (2019) 8928–8936.

[11] D. Wu, J. Guo, J. Du, C. Xia, L. Zeng, Y. Tian, Z. Shi, Y. Tian, X.J. Li, Y.H. Tsang, J. Jie, Highly polarization-sensitive, broadband, self-powered photodetector based on graphene/$PdSe_2$/germanium heterojunction, ACS Nano 13 (2019) 9907–9917.

[12] L.-H. Zeng, D. Wu, S.-H. Lin, C. Xie, H.-Y. Yuan, W. Lu, S.P. Lau, Y. Chai, L.-B. Luo, Z.-J. Li, Y.H. Tsang, Controlled synthesis of 2D palladium diselenide for sensitive photodetector applications, Adv. Funct. Mater. 29 (2019), 1806878.

[13] M. Long, Y. Wang, P. Wang, X. Zhou, H. Xia, C. Luo, S. Huang, G. Zhang, H. Yan, Z. Fan, X. Wu, X. Chen, W. Lu, W. Hu, Palladium diselenide long-wavelength infrared photodetector with high sensitivity and stability, ACS Nano 13 (2019) 2511–2519.

[14] Q. Liang, Q. Wang, Q. Zhang, J. Wei, S.X. Lim, R. Zhu, J. Hu, W. Wei, C. Lee, C. Sow, W. Zhang, A.T.S. Wee, High-performance, room temperature, ultra-broadband photodetectors based on air-stable $PdSe_2$, Adv. Mater. 31 (2019), 1807609.

[15] L. Pi, C. Hu, W. Shen, L. Li, P. Luo, X. Hu, P. Chen, D. Li, Z. Li, X. Zhou, T. Zhai, Highly in-plane anisotropic 2D $PdSe_2$ for polarized photodetection with orientation selectivity, Adv. Funct. Mater. 31 (2021), 2006774.

[16] J. Liang, Y. Yang, J. Zhang, J. Wu, P. Dong, J. Yuan, G. Zhang, J. Lou, Metal diselenide nanoparticles as highly active and stable electrocatalysts for the hydrogen evolution reaction, Nanoscale 7 (2015) 14813–14816.

[17] Q. Liang, Q. Zhang, J. Gou, T. Song, H. Arramel, M. Chen, S.X. Yang, Q. Lim, R. Wang, N. Zhu, S.C. Yakovlev, W. Tan, K.S. Zhang, A.T.S.W. Novoselov, Performance improvement by ozone treatment of 2D $PdSe_2$, ACS Nano 14 (2020) 5668–5677.

[18] Y. Zhao, P. Yu, G. Zhang, M. Sun, D. Chi, K. Hippalgaonkar, J.T.L. Thong, J. Wu, Low-symmetry $PdSe_2$ for high performance thermoelectric applications, Adv. Funct. Mater. 30 (2020), 2004896.

[19] Y. Li, L. Loh, S. Li, L. Chen, B. Li, M. Bosman, K.-W. Ang, Anomalous resistive switching in memristors based on two-dimensional palladium diselenide using heterophase grain boundaries, Nat. Electron. 4 (2021) 348–356.

[20] J. Yu, X. Kuang, J. Li, J. Zhong, C. Zeng, L. Cao, Z. Liu, Z. Zeng, Z. Luo, T. He, A. Pan, Y. Liu, Giant nonlinear optical activity in two-dimensional palladium diselenide, Nat. Commun. 12 (2021) 1083.

[21] J. Zhou, J. Lin, X. Huang, Y. Zhou, Y. Chen, J. Xia, H. Wang, Y. Xie, H. Yu, J. Lei, D. Wu, F. Liu, Q. Fu, Q. Zeng, C.-H. Hsu, C. Yang, L. Lu, T. Yu, Z. Shen, H. Lin, B. I. Yakobson, Q. Liu, K. Suenaga, G. Liu, Z. Liu, A library of atomically thin metal chalcogenides, Nature 556 (2018) 355–359.

[22] S. Jiang, C. Xie, Y. Gu, Q. Zhang, X. Wu, Y. Sun, W. Li, Y. Shi, L. Zhao, S. Pan, P. Yang, Y. Huan, D. Xie, Q. Zhang, X. Liu, X. Zou, L. Gu, Y. Zhang, Anisotropic growth and scanning tunneling microscopy identification of ultrathin even-layered $PdSe_2$ ribbons, Small 15 (2019), 1902789.

[23] L.-S. Lu, G.-H. Chen, H.-Y. Cheng, C.-P. Chuu, K.-C. Lu, C.-H. Chen, M.-Y. Lu, T.-H. Chuang, D.-H. Wei, W.-C. Chueh, W.-B. Jian, M.-Y. Li, Y.-M. Chang, L.-J. Li, W.-H. Chang, Layer-dependent and in-plane anisotropic properties of low-temperature synthesized few-layer $PdSe_2$ single crystals, ACS Nano 14 (2020) 4963–4972.

[24] Y. Gu, H. Cai, J. Dong, Y. Yu, A.N. Hoffman, C. Liu, A.D. Oyedele, Y.-C. Lin, Z. Ge, A.A. Puretzky, G. Duscher, M.F. Chisholm, P.D. Rack, C.M. Rouleau, Z. Gai, X. Meng, F. Ding, D.B. Geohegan, K. Xiao, Two-dimensional palladium diselenide with strong in-plane optical anisotropy and high mobility grown by chemical vapor deposition, Adv. Mater. 32 (2020), 1906238.

[25] W. Xu, J. Jiang, H. Ma, Z. Zhang, J. Li, B. Zhao, R. Wu, X. Yang, H. Zhang, B. Li, W. Shu, Z. Zhang, B. Li, Y. Liu, L. Liao, X. Duan, Vapor phase growth of two-dimensional $PdSe_2$ nanosheets for high-photoresponsivity near-infrared photodetectors, Nano Res. 13 (2020) 2091–2097.

[26] D. Hu, T. Zhao, X. Ping, H. Zheng, L. Xing, X. Liu, J. Zheng, L. Sun, L. Gu, C. Tao, D. Wang, L. Jiao, Unveiling the layer-dependent catalytic activity of $PtSe_2$ atomic crystals for the hydrogen evolution reaction, Angew. Chem. Int. Ed. 58 (2019) 6977–6981.

[27] X. Chia, A. Adriano, P. Lazar, Z. Sofer, J. Luxa, M. Pumera, Layered platinum dichalcogenides (PtS_2, $PtSe_2$, and $PtTe_2$) electrocatalysis: Monotonic dependence on the chalcogen size, Adv. Funct. Mater. 26 (2016) 4306–4318.

[28] J. Shi, Y. Huan, M. Hong, R. Xu, P. Yang, Z. Zhang, X. Zou, Y. Zhang, Chemical vapor deposition grown large-scale atomically thin platinum diselenide with semimetal−semiconductor transition, ACS Nano 13 (2019) 8442–8451.

[29] A.A. Puretzky, A.D. Oyedele, K. Xiao, A.V. Haglund, B.G. Sumpter, D. Mandrus, D. B. Geohegan, L. Liang, Anomalous interlayer vibrations in strongly coupled layered $PdSe_2$, 2D Mater. 5 (2018), 035016.

[30] J. Shi, P. Yu, F. Liu, P. He, R. Wang, L. Qin, J. Zhou, X. Li, J. Zhou, X. Sui, S. Zhang, Y. Zhang, Q. Zhang, T.C. Sum, X. Qiu, Z. Liu, X. Liu, 3R MoS_2 with broken inversion symmetry: A promising ultrathin nonlinear optical device, Adv. Mater. 29 (2017), 1701486.

NANO LETTERS

pubs.acs.org/NanoLett

Letter

Pressure-Enhanced Ferromagnetism in Layered $CrSiTe_3$ Flakes

Cheng Zhang, Yue Gu, Le Wang, Liang-Long Huang, Ying Fu, Cai Liu, Shanmin Wang,* Huimin Su, Jia-Wei Mei,* Xiaolong Zou,* and Jun-Feng Dai*

Cite This: https://doi.org/10.1021/acs.nanolett.1c01994

Read Online

ACCESS | Metrics & More | Article Recommendations | Supporting Information

ABSTRACT: Despite recent advances in layered ferromagnets, ferromagnetic interactions in these materials are rather weak. Here, we report pressure-enhanced ferromagnetism in layered $CrSiTe_3$ flakes revealed by high-pressure magnetic circular dichroism measurements. Below ~3 GPa, $CrSiTe_3$ undergoes a paramagnetic-to-ferromagnetic phase transition at ~32 K, and the field-induced spin−flip in the ferromagnetic phase produces nearly zero hysteresis loops, demonstrating soft ferromagnetism. Above ~4 GPa, a soft-to-hard ferromagnetic transition occurs, signaled by rectangular-shaped hysteresis loops with finite coercivity and remanent magnetization. Interestingly, as pressure increases, the Curie temperature and coercivity dramatically increase up to ~138 K and 0.17 T at 7.8 GPa, respectively, in contrast to ~36 K and 0.02 T at 4.6 GPa. It indicates a remarkable influence of pressure on exchange interactions, which is consistent with DFT calculations. The effective interaction between magnetic couplings and external pressure offers new opportunities in pursuit of high-temperature layered ferromagnets.

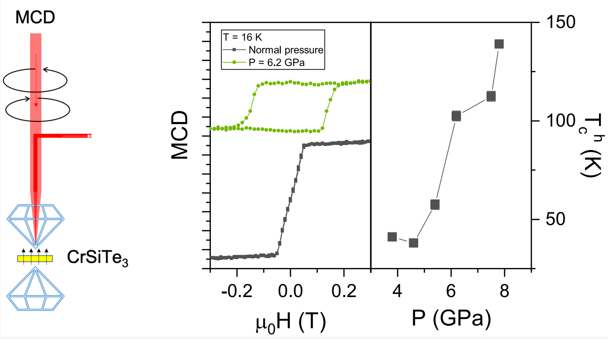

KEYWORDS: *2D ferromagnetic materials, exchange interaction, high-pressure magnetic circular dichroism (MCD) spectroscopy, magnetization*

Recently, layered ferromagnets coupled by van der Waals (vdW) force, such as $CrGeTe_3$,[1] CrI_3,[2] and Fe_3GeTe_2,[3,4] have gained significant interest because they provide an ideal platform for the study of the fundamental magnetic interactions in the two-dimensional (2D) limit. So far, the intrinsic Curie temperatures (T_c) of known 2D ferromagnets are still not sufficiently high (CrI_3, 45K; $GrGeTe_3$, 30 K; Fe_3GeTe_2, 68 K);[1−3] hence, considerable efforts have been devoted to increasing their T_c and making the long-range ferromagnetism more robust. Naturally, enhancing the ferromagnetic exchange interaction can contribute to the increase of T_c.[5] Besides, for 2D ferromagnets, magnetocrystalline anisotropy breaks the spin-rotational symmetry and can also stabilize 2D Ising-type ferromagnetism. Therefore, searching for new routes to improve magnetic interactions is of great significance to the fundamental research of 2D ferromagnets.

Compared to those in bulk counterparts, the magnetic states of 2D ferromagnets show greater controllability by external stimuli,[3,6−11] which may improve their exchange interactions, thereby deepening our understanding of the underlying mechanisms of magnetism in 2D systems. In this regard, hydrostatic pressure is one of the direct routes for dynamically modifying both the crystal and band structures of materials.[12−16] It can effectively tune the distance between adjacent atomic layers, as well as bond lengths and bond angles of intralayer atoms in 2D magnets, leading to modulation of interlayer and intralayer exchange interactions. Experimentally, in bilayer CrI_3,[7,17] hydrostatic pressure can switch the magnetic orders between antiferromagnetic and ferromagnetic states. Under pressure, Fe_3GeTe_2 shows the reduction of the local moment on Fe ions as well as the increase of the electronic itinerancy.[18,19] In addition, a spin reorientation has also been reported in the layered ferromagnetic insulator $CrGeTe_3$ under pressure,[20] highlighting the effective control of magnetocrystalline anisotropy by pressure. However, to date, pressure-induced enhancement of Curie temperature and coercive field in 2D magnets has rarely been reported.

$CrSiTe_3$, isotypic as $CrGeTe_3$ (Figure 1a), exhibits soft ferromagnetic behaviors without involving a remanent magnetization at zero field.[21] After the replacement of Ge by smaller Si, the application of hydrostatic pressure should further shorten the distance between 3d atoms. Therefore, the exchange interactions and the magnetic behaviors could be

Received: May 21, 2021

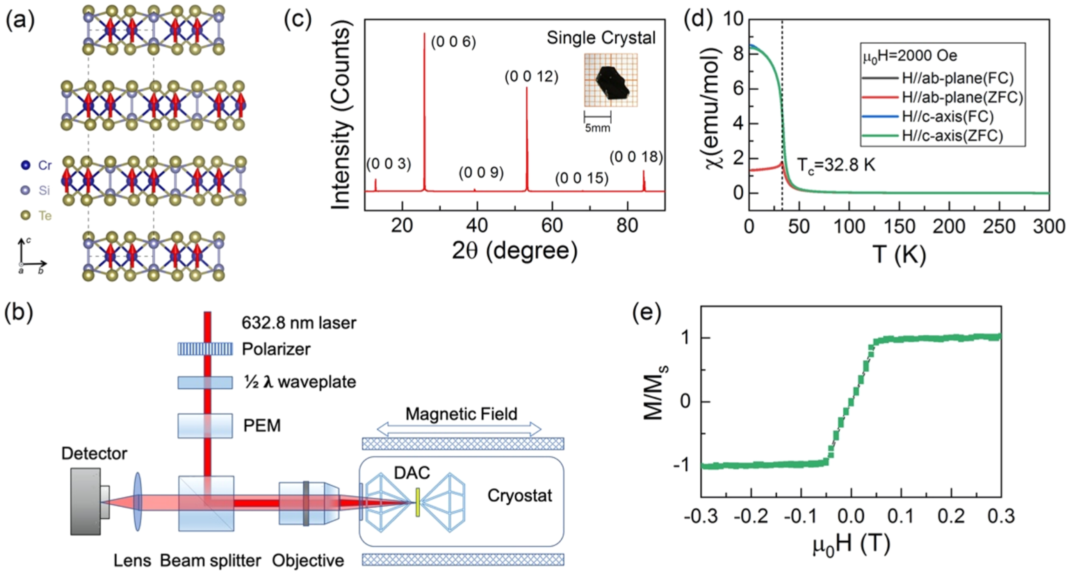

Figure 1. (a) Side view of the crystal structure of $CrSiTe_3$. Red arrows indicate the spin orientation. (b) Schematic diagram of in situ high-pressure magnetic circular dichroism (MCD) experimental setup with the lowest temperature of 16 K and the highest pressure of 12 GPa, respectively. (c) Single-crystal X-ray diffraction pattern of $CrSiTe_3$. The inset is an optical image of single-crystal $CrSiTe_3$. (d) Magnetic susceptibility of $CrSiTe_3$ measured on a single crystal with both the field cooling (FC) and zero-field cooling (ZFC) modes under a magnetic field of 2000 Oe applied along the *c*-axis and *ab*-plane, respectively. (e) Magnetization of a $CrSiTe_3$ flake as a function of magnetic field (H) along the *c*-axis, measured at 16 K and ambient pressure.

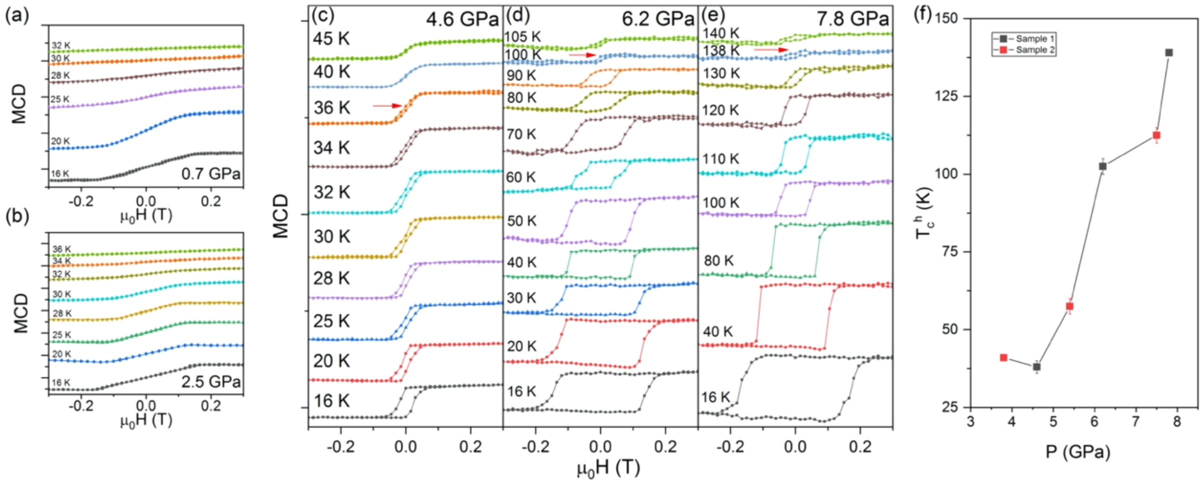

Figure 2. Temperature dependence of MCD signals in the $CrSiTe_3$ flake under five fixed pressures, namely, (a) 0.7, (b) 2.5, (c) 4.6, (d) 6.2, and (e) 7.8 GPa, respectively. Red arrows indicate the temperature for closure of the hysteresis loop at 4.6, 6.2, and 7.8 GPa, respectively. (f) Curie temperature (T_c^h) extracted from temperature-dependent MCD measurements in sample 1 (black squares) and sample 2 (red squares), respectively. Temperature dependence of MCD signals in sample 2 is shown in Figure S3.

greatly influenced given the small band gap of $CrSiTe_3$.[22] Meanwhile, a recent report showed that ferromagnetic $CrSiTe_3$ undergoes a transition to the superconducting phase under a pressure of ~7.5 GPa,[23] which makes a detailed understanding of the pressure-induced evolution of magnetic behaviors very important. In this work, we investigate the ferromagnetic properties of $CrSiTe_3$ flakes under pressure up to 10 GPa, using in situ high-pressure magnetic circular dichroism (MCD) microscopy. We observe a ferromagnetic-like hysteresis loop at a pressure of ~4 GPa, indicating a transition from soft to hard ferromagnetic states. Importantly, a further increase of pressure up to 7.8 GPa dramatically increases both the Curie temperature (T_c^h, the temperature for closing the hysteresis loop) and coercive field (H_c). Our density functional theory (DFT) calculations reveal an enhancement of the in-plane nearest-neighbor exchange interaction (J_1) as pressure increases, corroborating the experimental observations.

Experimental Setup. High-pressure experiments were performed in a diamond-anvil cell (DAC) with pressure up to around 10 GPa. To load the sample into DAC, we first mechanically exfoliated $CrSiTe_3$ flakes from signal crystal with a size larger than 50 μm × 50 μm. The sample thickness was at the nanometer scale (~100 nm). Then they were transferred onto one culet of diamond using polycarbonate (PC) films. The entire sample was then covered by BN flakes to prevent sample degradation. After filling the pressure-transmitting medium and ruby balls, the entire DAC was mounted onto the coldfinger of the low-temperature cryostat operating over a temperature range from 16 to 300 K. The out-of-plane ferromagnetic states were probed using in situ high-pressure MCD spectroscopy, as schematically illustrated in Figure 1b. More experimental details about this technique can be found in Methods.

Experimental Results. $CrSiTe_3$ single crystals were grown by the flux method (see Methods for details). The representative sample size was around 5 × 7 mm^2 as shown in the inset of Figure 1c. $CrSiTe_3$ has a layered honeycomb structure coupled with van der Waals (vdW) force (Figure 1a). The X-ray diffraction (XRD) results in Figure 1c and Figure S1 indicate the high quality of our sample. The magnetic susceptibility (χ) measurement in Figure 1d reveals a ferromagnetic (FM) transition with the Curie temperature (T_c) about 32.8 K at an ambient pressure. The value of χ_c is four times larger than χ_{ab} at 2 K, which suggests that the crystallographic *c*-axis is the easy axis, consistent with the previous report.[24] The MCD measurement also shows a saturation magnetization as the applied field increases above 0.05 T at 16 K (Figure 1e and Figure S2). However, there is no hysteresis loop in the MCD measurement when we sweep the field back and forth. It indicates a soft ferromagnetic behavior in bulk $CrSiTe_3$, resembling that of $CrGeTe_3$[9]. Overall, at an ambient pressure, $CrSiTe_3$ exhibits a quasi-2D Ising ferromagnetic order below a Curie temperature of ∼32.8 K with a negligible coercivity.

We first characterize the magnetic behaviors of layered $CrSiTe_3$ under pressures by the temperature-dependent MCD measurements. Figure 2 shows the signals as a function of the applied field in sample 1 across a range of temperatures for five fixed hydrostatic pressures. At 0.7 and 2.5 GPa, the magnetic behavior of $CrSiTe_3$ is characterized by a linear relationship between the magnetization and the applied magnetic field below ±0.15 T and a saturation magnetization above that value. As the temperature increases, the MCD signals gradually change to a pure linear response to the field without any saturation magnetization within ±0.3 T. This indicates a transition from ferromagnetic to paramagnetic states. One interesting observation is that the extracted transition temperature for two low-pressure cases barely changes compared to that without pressure, i.e., ∼ 32 K at 0.7 GPa (Figure 2a) and ∼34 K at 2.5 GPa (Figure 2b), respectively. Results from another sample (sample 2, see Figure S3) show similar behaviors, where the transition temperature is ∼32 K at both 1.1 and 2.9 GPa. The negligible change of transition temperature indicates the weak influence of pressure on magnetic behavior at low pressure.

Surprisingly, when the pressure increases to 4.6 GPa, a hysteresis loop develops at low temperatures and sustains until 40 K (Figure 2c). The appearance of remanent magnetic order at zero field indicates that the corresponding magnetic state of $CrSiTe_3$ is a hard ferromagnetic one. In these cases, we define the temperature for the closure of the hysteresis loop as the Curie temperature (T_c^h). As pressure increases further, the hysteresis loop can survive up to even higher temperatures, where T_c^h is evaluated to be ∼100 K at 6.2 GPa (Figure 2d) and ∼138 K at 7.8 GPa (Figure 2e), respectively. Similarly, for sample 2, T_c^h increases from ∼41 K at 3.8 GPa to ∼110 K at 7.5 GPa (Figure S3). The T_c^h values extracted from two samples are summarized in Figure 2f, which shows a remarkable increase as pressure increases. Although it changes little under low pressures, the ferromagnetism in layered $CrSiTe_3$ under high pressures is significantly enhanced.

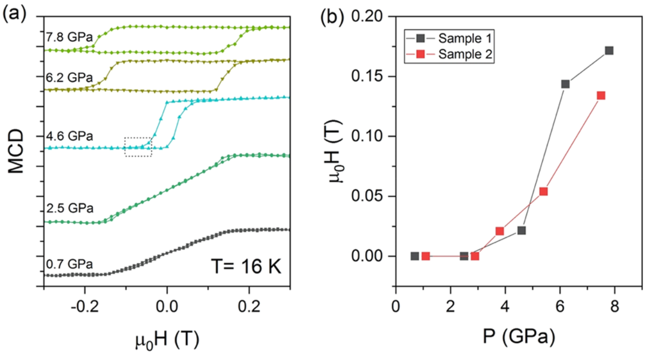

Figure 3. (a) MCD signals as a function of the applied magnetic field in sample 1 at 16 K as pressure changes from 0.7 to 7.8 GPa. The dashed square indicates the deviation from a rectangular hysteresis loop. (b) Extracted average critical field for the spin−flip transition as a function of applied pressure. The black and red squares are extracted from samples 1 and 2, respectively.

Besides the enhanced T_c^h, we observe a substantial change in hysteresis loops accompanied by the development of the finite coercive field, as summarized for sample 1 at a selected temperature (16 K) under five fixed hydrostatic pressures (Figure 3a). At low pressures (0.7 and 2.5 GPa), the magnetization linearly increases with the applied magnetic field and then saturates above 0.15 T due to spin−spin exchange interaction. Importantly, the negligible hysteresis loop in MCD signals with zero remanent magnetization at $\mu_0 H = 0\ T$ suggests that the barrier between two spin-polarized states is very low. So this is also considered as a soft ferromagnetic state for these two low-pressure cases. A similar soft ferromagnetic behavior is also found in sample 2 at 1.1 and 2.9 GPa (Figure S3). Under 4.6 GPa, a typical hysteresis loop with a finite coercive field appears as the applied field was swept in the range of −0.3 to 0.3 T. However, as indicated by the dashed square in Figure 3a, the hysteresis loops at high pressure do not show a standard rectangular shape, indicative of the influence of the labyrinthine domain.[4,25] The average coercive field under 4.6 GPa is evaluated to be 0.02 T at 16 K. As pressure increases further, the hysteresis loop changes to a rectangular shape with enlarged areas, and the corresponding coercive field also increases to 0.17 T at 7.8 GPa. For sample 2, the coercive field increases from 0.021 T at 3.8 GPa to 0.134 T at 7.5 GPa. The extracted coercive field from samples 1 and 2 in Figure 3b shows a dramatic increase as pressure increases from a threshold pressure of around 4 GPa to around 7.8 GPa. Above 7.8 GPa, we cannot detect any MCD signal due to a structural transition at ∼7.5 GPa accompanied by a ferromagnetic-paramagnetic phase transition[11] (data are not shown). A pressure-induced insulator−metal transition in $CrSiTe_3$ and $CrGeTe_3$ has been reported previously.[23,26] Although we did not directly observe such an insulator−metal transition, we notice that the pressure-dependent Raman measurements (Figure S4) also reveal negligible peaks above 7.8 GPa at room temperature, consistent with a metallic state in $CrSiTe_3$.

Theoretical Simulations. To further understand two key observations in experiments, DFT calculations were employed to investigate the response of structural, electronic, and magnetic properties of $CrSiTe_3$ to external pressure. $CrSiTe_3$ crystallizes in the $R\bar{3}$space group, with the monolayers stacked in an ABCABC sequence, as shown in Figure 1a. To describe

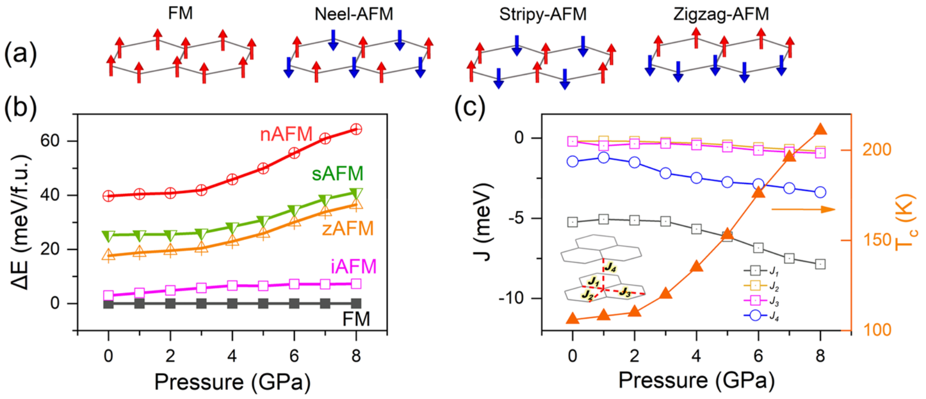

Figure 4. (a) Schematics for ferromagnetic and three antiferromagnetic orders: Néel-AFM, Stripy-AFM, and Zigzag-AFM. (b) The calculated energy difference between different magnetic orders and ground FM state as a function of pressure. (c) Calculated intralayer first, second, and third nearest-neighbor exchange interactions J_1, J_2, J_3, interlayer nearest-neighbor exchange interactions J_4 (illustrated in the insets), and Curie temperature T_c as functions of pressure.

the possible structural transition, we also consider two other stacking orders, i.e., AA and inclined AA sequences illustrated in the insets of Figure S5, both of which correspond to the $C2/m$ space group. The energies of these three structures as a function of pressure are shown in Figure S5. It is noted that even when the pressure increases to 12 GPa, the energies of two $C2/m$ phases are still higher than that of the $R\bar{3}$ phase. Therefore, we focus on the $R\bar{3}$ phase hereafter.

We have considered various magnetic states, including ferromagnetic (FM) state, interlayer antiferromagnetic (AFM) state with intralayer FM coupling, and three intralayer AFM states with interlayer FM coupling. The four AFM states are named interlayer-AFM (iAFM), Néel-AFM (nAFM), Stripy-AFM (sAFM), and Zigzag-AFM (zAFM), respectively, with the last three states shown in Figure 4a, according to their different intralayer arrangements for local magnetic moments. The calculated pressure-dependent energies for these states by the DFT+U method are displayed in Figure 4b, which clearly shows that FM order is always the ground state. More importantly, the energy difference between FM and AFM orders generally increases as pressure increases, which suggests that the stability of ferromagnetism is enhanced by pressure.

To quantitatively estimate T_c of $CrSiTe_3$ under pressure, we adopted Monte Carlo (MC) simulations based on the Heisenberg Hamiltonian $H = \sum_{i<j} J_{ij} \mathbf{S}_i \cdot \mathbf{S}_j + A \sum_{i} (\mathbf{S}_i^z)^2 + \sum_{i<j} B_{ij} \mathbf{S}_i^z \cdot \mathbf{S}_j^z$,[27] where S_i is the spin operator of Cr on site i (~3/2 in our case), J_{ij} and B_{ij} are the exchange coupling constant and anisotropic exchange constant between spins on sites i and j, and A is the single-ion anisotropy constant. For exchange interactions, the intralayer first, second, and third nearest-neighbor exchange terms, J_i and B_i ($i = 1, 2, 3$), as well as the interlayer first nearest-neighbor exchange interaction, J_4 and B_4, were considered, with J_1 to J_4 illustrated in the insets of Figure 4c. All considered parameters calculated from the energies of different magnetic orders are shown in Table S1, which shows that the strength of B's is significantly smaller than J's. The variation of J's against pressure is shown in Figure 4c. It can be seen that all these J's are always negative, which tends to stabilize FM order. The absolute values of J_1 and J_4 are much larger than those of J_2 and J_3, with J_1 always stronger than J_4. Given that the number of neighboring sites for J_1 ($n = 3$) is larger than that for J_4 ($n = 1$), the contribution of J_1 in the Hamiltonian is much greater than J_4. Therefore, the intralayer first nearest-neighbor exchange interaction J_1 plays a dominant role in the enhancement of ferromagnetism. MC simulations show that T_c increases rapidly, from ~100 K without pressure to ~210 K under 8 GPa. Although MC results overestimate T_c, the obtained variation of T_c is consistent with our experimental results from 0 to 7.8 GPa. The pressure-induced enhancement of the FM interaction under pressure can be qualitatively understood by the change in the virtual hopping gap between spin-up unoccupied e_g and occupied t_{2g} orbitals, which shows a monotonic decrease with increasing pressure (Figure S7), giving rise to enhanced FM exchange coupling.[28]

Regarding the coercive field H_c, it is proportional to the ratio of magnetic anisotropy to magnetization.[5] Although the magnetic anisotropy energy can be reliably assessed by DFT simulations, it is challenging to accurately predict the magnetization because of the pressure-induced insulator—metal transition in $CrSiTe_3$, which implies that the nature of the magnetic moments of the 3d electrons on Cr^{3+} changes from local to itinerant. The evolution of band structures under pressure is shown in Figure S6, along with the orbital projection of Cr and Te atoms. The top valence bands and bottom conduction bands are contributed by Te atoms and hybrid orbitals from Cr and Te atoms, respectively. Under pressure, top valence bands shift up significantly, and bottom conduction bands move down slightly, giving rise to the metallicity. As the system approaches the insulator-to-metal transition, strong many-body effects arise, leading to reduced magnetic moment for the 3d electron on Cr^{3+}, which is indeed observed in a similar compound, $CrGeTe_3$, under pressure.[26] The reduced magnetic moment is probably due to the coupling between localized moments and itinerant electrons. Considering the nearly constant magnetic anisotropy from DFT calculations (Figure S8), this, in turn, leads to an enhancement of the ratio between anisotropy and magnetization and thus the increase of the coercive field.

In conclusion, the ferromagnetic properties of $CrSiTe_3$ flakes under pressure have been carefully investigated, based on in situ high-pressure MCD measurements and theoretical calculations. We find that $CrSiTe_3$ is a soft ferromagnet at low pressures and transforms into a hard ferromagnet above ~4 GPa with a profoundly enhanced Curie temperature up to ~138 K at 7.8 GPa. In addition, the coercivity of the hard ferromagnetic phase also has a strong pressure dependence.

Our calculations show that these pressure-induced magnetic phenomena in $CrSiTe_3$ are primarily associated with the in-plane nearest-neighbor exchange interaction. The findings of this work are important for understanding the underlying mechanism of the magnetic exchange interaction and open up a novel route for effectively tuning the magnetic properties of 2D materials.

Methods. *Sample Growth.* $CrSiTe_3$ crystals were grown by using the Si−Te eutectic as flux. High-purity elements Cr grains (99.996%), Si pieces (99.9999%), and Te blocks (99.9999%) were weighed in the molar ratio Cr/Si/Te = 1:2:6, placed in an alumina crucible, and then sealed in a fully evacuated quartz tube. The crucible was heated to 1373 K, stored for 10 h, and then cooled slowly to 973 K in 150 h, where the flux was spun off by a centrifuge. The single-crystal XRD and powder (obtained by grounding the single crystals) XRD were performed on a Rigaku Smartlab-9 kW diffractometer with Cu Kα radiation ($\lambda_{K\alpha 1}$ = 1.54056 Å) at room temperature. The magnetic susceptibility (χ) measurements were carried out on a Quantum Design MPMS3 SQUID magnetometer.

High-Pressure Magnetic Circular Dichroism Measurements. The ferromagnetic behaviors of the $CrSiTe_3$ flake under high pressure were measured in an in situ magnetic circular dichroism (MCD) system (Figure 1b). A 632.8 nm HeNe laser was selected as an incident light source and focused onto the sample loaded within DAC by a long working distance objective with a spot size of around ~2 μm. The polarization state of the incident light beam was modulated by a photoelastic modulator (PEM) so that it changed between the left-handed and right-handed circular polarization with a frequency of 50 kHz. The reflected MCD signal, i.e., the intensity difference between two circularly polarized lights, was collected by a silicon detector and recorded by a lock-in amplifier. During measurements, the out-of-plane magnetic field that was generated from a superconducting loop was scanned within ±0.3 T. Hence, we can get the MCD signals of the sample as a function of the applied magnetic field.

Density Functional Theory (DFT) First-Principles Calculations. Our density functional theory (DFT) calculations were done adopting the Vienna ab initio Simulation Package (VASP),[29,30] with Perdew−Burke−Ernzerhof parametrization of the generalized gradient approximation (GGA)[31] and projector augmented wave (PAW) method,[32] describing the exchange-correlation and ion-electron interactions, respectively. A cutoff energy of 500 eV was chosen for the plane waves basis set. The structural optimization was performed until the force on each atom and energy were converged to 0.01 eV/Å and 1×10^{-6} eV, respectively. The van der Waals (vdW) interaction was included using the optB86b-vdW functional.[33] The DFT+U method was used to treat the onsite Coulomb interaction of Cr d orbitals properly.[34] Similar to $CrGeTe_3$,[1] the choice of Hubbard U is crucial to determine the electronic and magnetic properties of $CrSiTe_3$. We tested different values of U (Table S2) and finally chose U = 0.5 to ensure the appropriate ground magnetic state of $CrSiTe_3$, i.e., interlayer ferromagnetic coupling and the easy axis magnetization along the out-of-plane direction. With $6 \times 6 \times 2$ k-point sampling, the optimized bulk lattice constants are $a = b$ = 6.81 Å and c = 20.48 Å. A k-point mesh of $9 \times 9 \times 3$ is used for the calculations of exchange interactions to ensure convergence of energy (see Figure S9 for the test on magnetocrystalline anisotropy energy). Monte Carlo simulations based on the Metropolis algorithm were performed using the MCSOLVER code.[35]

ASSOCIATED CONTENT

Supporting Information

The Supporting Information is available free of charge at https://pubs.acs.org/doi/10.1021/acs.nanolett.1c01994.

Characteristic of $CrSiTe_3$ single crystals and DFT calculations (PDF)

AUTHOR INFORMATION

Corresponding Authors

Shanmin Wang − *Shenzhen Institute for Quantum Science and Engineering, and Department of Physics, Southern University of Science and Technology, Shenzhen 518055, China;* orcid.org/0000-0001-7273-2786; Email: wangsm@sustech.edu.cn

Jia-Wei Mei − *Shenzhen Institute for Quantum Science and Engineering, and Department of Physics, Southern University of Science and Technology, Shenzhen 518055, China; Shenzhen Key Laboratory of Advanced Quantum Functional Materials and Devices, Southern University of Science and Technology, Shenzhen 518055, China;* Email: meijw@sustech.edu.cn

Xiaolong Zou − *Shenzhen Geim Graphene Center, Tsinghua-Berkeley Shenzhen Institute & Tsinghua Shenzhen International Graduate School, Tsinghua University, Shenzhen 518055, China;* orcid.org/0000-0002-3987-6865; Email: xlzou@sz.tsinghua.edu.cn

Jun-Feng Dai − *Shenzhen Institute for Quantum Science and Engineering, and Department of Physics, Southern University of Science and Technology, Shenzhen 518055, China; Shenzhen Key Laboratory of Quantum Science and Engineering, Shenzhen 518055, China;* orcid.org/0000-0003-1600-8798; Email: daijf@sustech.edu.cn

Authors

Cheng Zhang − *School of Physics, Harbin Institute of Technology, Harbin 150001, China; Shenzhen Institute for Quantum Science and Engineering, and Department of Physics, Southern University of Science and Technology, Shenzhen 518055, China*

Yue Gu − *Shenzhen Geim Graphene Center, Tsinghua-Berkeley Shenzhen Institute & Tsinghua Shenzhen International Graduate School, Tsinghua University, Shenzhen 518055, China*

Le Wang − *Shenzhen Institute for Quantum Science and Engineering, and Department of Physics, Southern University of Science and Technology, Shenzhen 518055, China*

Liang-Long Huang − *Shenzhen Institute for Quantum Science and Engineering, and Department of Physics, Southern University of Science and Technology, Shenzhen 518055, China*

Ying Fu − *Shenzhen Institute for Quantum Science and Engineering, and Department of Physics, Southern University of Science and Technology, Shenzhen 518055, China*

Cai Liu − *Shenzhen Institute for Quantum Science and Engineering, and Department of Physics, Southern University of Science and Technology, Shenzhen 518055, China*

Huimin Su − *Shenzhen Institute for Quantum Science and Engineering, and Department of Physics, Southern University of Science and Technology, Shenzhen 518055, China*

Complete contact information is available at:
https://pubs.acs.org/10.1021/acs.nanolett.1c01994

Author Contributions

C.Z., Y.G., and L.W. contributed to this work equally. J.D., X.Z., and J.M. conceived the project. J.D., C.Z., and H.S. designed and performed the experiments. L.W., L.H., Y.F., and C.L. provided and characterized the samples. S.W. provided the DAC technique and designed the high-pressure experiments. Y.G. and X.Z. provided the theoretical supports. All authors discussed the results and cowrote the paper.

Notes

The authors declare no competing financial interest.

■ ACKNOWLEDGMENTS

We would like to thank Prof. Haizhou Lu from SUSTech for helpful discussions. J.F.D. acknowledges the support from the National Natural Science Foundation of China (11974159) and the Guangdong Natural Science Foundation (2021A1515012316). J.W.M. was partially supported by the program for Guangdong Introducing Innovative and Entrepreneurial Teams (2017ZT07C062) and Shenzhen Key Laboratory of Advanced Quantum Functional Materials and Devices (ZDSYS20190902092905285). J.W.M. and L.W. were supported by the Guangdong Basic and Applied Basic Research Foundation (2020B1515120100). L.W. was supported by the China Postdoctoral Science Foundation (2020M682780). S.W. was supported by the Key Research Platforms and Research Projects of Universities in Guangdong Province (2018KZDXM062). The theoretical part was supported by the National Natural Science Foundation of China (11974197 and 51920105002) and the Guangdong Innovative and Entrepreneurial Research Team Program (2017ZT07C341).

■ REFERENCES

(1) Gong, C.; Li, L.; Li, Z. L.; Ji, H. W.; Stern, A.; Xia, Y.; Cao, T.; Bao, W.; Wang, C. Z.; Wang, Y. A.; Qiu, Z. Q.; Cava, R. J.; Louie, S. G.; Xia, J.; Zhang, X. Discovery of intrinsic ferromagnetism in two-dimensional van der Waals crystals. *Nature* **2017**, *546* (7657), 265−269.

(2) Huang, B.; Clark, G.; Navarro-Moratalla, E.; Klein, D. R.; Cheng, R.; Seyler, K. L.; Zhong, D.; Schmidgall, E.; McGuire, M. A.; Cobden, D. H.; Yao, W.; Xiao, D.; Jarillo-Herrero, P.; Xu, X. D. Layer-dependent ferromagnetism in a van der Waals crystal down to the monolayer limit. *Nature* **2017**, *546* (7657), 270−273.

(3) Deng, Y. J.; Yu, Y. J.; Song, Y. C.; Zhang, J. Z.; Wang, N. Z.; Sun, Z. Y.; Yi, Y. F.; Wu, Y. Z.; Wu, S. W.; Zhu, J. Y.; Wang, J.; Chen, X. H.; Zhang, Y. B. Gate-tunable room-temperature ferromagnetism in two-dimensional Fe3GeTe2. *Nature* **2018**, *563* (7729), 94−99.

(4) Fei, Z. Y.; Huang, B.; Malinowski, P.; Wang, W. B.; Song, T. C.; Sanchez, J.; Yao, W.; Xiao, D.; Zhu, X. Y.; May, A. F.; Wu, W. D.; Cobden, D. H.; Chu, J. H.; Xu, X. D. Two-dimensional itinerant ferromagnetism in atomically thin Fe3GeTe2. *Nat. Mater.* **2018**, *17* (9), 778−782.

(5) Siegmann, J. S. a. H. C. *Magnetism: From Fundamentals to Nanoscale Dynamics*; Springer: Berlin, NY, 2006; pp 491−494.

(6) Mondal, S.; Kannan, M.; Das, M.; Govindaraj, L.; Singha, R.; Satpati, B.; Arumugam, S.; Mandal, P. Effect of hydrostatic pressure on ferromagnetism in two-dimensional CrI3. *Phys. Rev. B: Condens. Matter Mater. Phys.* **2019**, *99* (18), 180407.

(7) Song, T. C.; Fei, Z. Y.; Yankowitz, M.; Lin, Z.; Jiang, Q. N.; Hwangbo, K.; Zhang, Q.; Sun, B. S.; Taniguchi, T.; Watanabe, K.; McGuire, M. A.; Graf, D.; Cao, T.; Chu, J. H.; Cobden, D. H.; Dean, C. R.; Xiao, D.; Xu, X. D. Switching 2D magnetic states via pressure tuning of layer stacking. *Nat. Mater.* **2019**, *18* (12), 1298−1302.

(8) Subhan, F.; Khan, I.; Hong, J. S. Pressure-induced ferromagnetism and enhanced perpendicular magnetic anisotropy of bilayer CrI3. *J. Phys.: Condens. Matter* **2019**, *31* (35), 355001.

(9) Verzhbitskiy, I. A.; Kurebayashi, H.; Cheng, H. X.; Zhou, J.; Khan, S.; Feng, Y. P.; Eda, G. Controlling the magnetic anisotropy in Cr2Ge2Te6 by electrostatic gating. *Nat. Electron* **2020**, *3* (8), 460−465.

(10) Zhang, S.; Xu, R.; Luo, N.; Zou, X. Two-dimensional magnetic materials: structures, properties and external controls. *Nanoscale* **2021**, *13* (3), 1398−1424.

(11) Gu, Y.; Zhang, S.; Zou, X. Tunable magnetism in layered CoPS3 by pressure and carrier doping. *Science China Materials* **2021**, *64* (3), 673−682.

(12) Yankowitz, M.; Jung, J.; Laksono, E.; Leconte, N.; Chittari, B. L.; Watanabe, K.; Taniguchi, T.; Adam, S.; Graf, D.; Dean, C. R. Dynamic band-structure tuning of graphene moiré superlattices with pressure. *Nature* **2018**, *557* (7705), 404−408.

(13) Fu, L.; Wan, Y.; Tang, N.; Ding, Y.-m.; Gao, J.; Yu, J.; Guan, H.; Zhang, K.; Wang, W.; Zhang, C.; Shi, J.-j.; Wu, X.; Shi, S.-F.; Ge, W.; Dai, L.; Shen, B. K-Λ crossover transition in the conduction band of monolayer MoS_2 under hydrostatic pressure. *Science Advances* **2017**, *3* (11), No. e1700162.

(14) Xia, J.; Yan, J.; Wang, Z.; He, Y.; Gong, Y.; Chen, W.; Sum, T. C.; Liu, Z.; Ajayan, P. M.; Shen, Z. Strong coupling and pressure engineering in WSe2−MoSe2 heterobilayers. *Nat. Phys.* **2021**, *17* (1), 92−98.

(15) Zhang, L.; Tang, Y.; Khan, A. R.; Hasan, M. M.; Wang, P.; Yan, H.; Yildirim, T.; Torres, J. F.; Neupane, G. P.; Zhang, Y.; Li, Q.; Lu, Y. 2D Materials and Heterostructures at Extreme Pressure. *Advanced Science* **2020**, *7* (24), 2002697.

(16) Su, H.; Liu, X.; Wei, C.; Li, J.; Sun, Z.; Liu, Q.; Zhou, X.; Deng, J.; Yi, H.; Hao, Q.; Zhao, Y.; Wang, S.; Huang, L.; Wu, S.; Zhang, W.; Li, G.; Dai, J.-F. Pressure-Controlled Structural Symmetry Transition in Layered InSe. *Laser Photonics Rev.* **2019**, *13* (6), 1900012.

(17) Li, T.; Jiang, S.; Sivadas, N.; Wang, Z.; Xu, Y.; Weber, D.; Goldberger, J. E.; Watanabe, K.; Taniguchi, T.; Fennie, C. J.; Fai Mak, K.; Shan, J. Pressure-controlled interlayer magnetism in atomically thin CrI3. *Nat. Mater.* **2019**, *18* (12), 1303−1308.

(18) Wang, H. S.; Xu, R. Z.; Liu, C.; Wang, L.; Zhang, Z.; Su, H. M.; Wang, S. M.; Zhao, Y. S.; Liu, Z. J.; Yu, D. P.; Mei, J. W.; Zou, X. L.; Dai, J. F. Pressure-Dependent Intermediate Magnetic Phase in Thin Fe3GeTe2 Flakes. *J. Phys. Chem. Lett.* **2020**, *11* (17), 7313−7319.

(19) Wang, X. Q.; Li, Z. Y.; Zhang, M.; Hou, T.; Zhao, J. G.; Li, L.; Rahman, A.; Xu, Z. L.; Gong, J. B.; Chi, Z. H.; Dai, R. C.; Wang, Z. P.; Qiao, Z. H.; Zhang, Z. M. Pressure-induced modification of the anomalous Hall effect in layered Fe3GeTe2. *Phys. Rev. B: Condens. Matter Mater. Phys.* **2019**, *100* (1), 1−6.

(20) Lin, Z. S.; Lohmann, M.; Ali, Z. A.; Tang, C.; Li, J. X.; Xing, W. Y.; Zhong, J. N.; Jia, S.; Han, W.; Coh, S.; Beyermann, W.; Shi, J. Pressure-induced spin reorientation transition in layered ferromagnetic insulator Cr2Ge2Te6. *Phys. Rev. Mater.* **2018**, *2* (5), 1−6.

(21) Liu, B. J.; Zou, Y. M.; Zhang, L.; Zhou, S. M.; Wang, Z.; Wang, W. K.; Qu, Z.; Zhang, Y. H. Critical behavior of the quasi-two-dimensional semiconducting ferromagnet CrSiTe3. *Sci. Rep.* **2016**, *6*, 2−9.

(22) Casto, L. D.; Clune, A. J.; Yokosuk, M. O.; Musfeldt, J. L.; Williams, T. J.; Zhuang, H. L.; Lin, M. W.; Xiao, K.; Hennig, R. G.; Sales, B. C.; Yan, J. Q.; Mandrus, D. Strong spin-lattice coupling in CrSiTe3. *APL Mater.* **2015**, *3* (4), 041515.

(23) Cai, W. P.; Sun, H. L.; Xia, W.; Wu, C. W.; Liu, Y.; Liu, H.; Gong, Y.; Yao, D. X.; Guo, Y. F.; Wang, M. Pressure-induced superconductivity and structural transition in ferromagnetic CrSiTe3. *Phys. Rev. B: Condens. Matter Mater. Phys.* **2020**, *102* (14), 1−7.

(24) Carteaux, V.; Moussa, F.; Spiesser, M. 2d Ising-Like Ferromagnetic Behavior for the Lamellar Cr2Si2Te6 Compound: A Neutron-Scattering Investigation. *Europhys. Lett.* **1995**, *29* (3), 251−256.

(25) Wu, S.; Wang, L.; Gao, B.; Wang, Y.; Oh, Y. S.; Cheong, S.-W.; Hong, J.; Wang, X. The direct observation of ferromagnetic domain of single crystal CrSiTe3. *AIP Adv.* **2018**, *8* (5), 055016.

(26) Bhoi, D.; Gouchi, J.; Hiraoka, N.; Zhang, Y.; Ogita, N.; Hasegawa, T.; Kitagawa, K.; Takagi, H.; Kim, K.-H.; Uwatoko, Y. *Nearly room temperature ferromagnetism in pressure-induced correlated metallic state of van der Waals insulator CrGeTe3*. arXiv 2021, 2107.10573. https://arxiv.org/abs/2107.10573 (accessed Jul 22, 2021).

(27) Torelli, D.; Olsen, T. Calculating critical temperatures for ferromagnetic order in two-dimensional materials. *2D Mater.* **2019**, *6* (1), 015028.

(28) Khomskii, D. *Transition metal compounds*; Cambridge University Press: Cambridge, 2014; p 122.

(29) Kresse, G.; Furthmuller, J. Efficient iterative schemes for ab initio total-energy calculations using a plane-wave basis set. *Phys. Rev. B: Condens. Matter Mater. Phys.* **1996**, *54* (16), 11169−11186.

(30) Kresse, G.; Furthmuller, J. Efficiency of ab-initio total energy calculations for metals and semiconductors using a plane-wave basis set. *Comput. Mater. Sci.* **1996**, *6* (1), 15−50.

(31) Perdew, J. P.; Burke, K.; Ernzerhof, M. Generalized gradient approximation made simple. *Phys. Rev. Lett.* **1996**, *77* (18), 3865−3868.

(32) Kresse, G.; Joubert, D. From ultrasoft pseudopotentials to the projector augmented-wave method. *Phys. Rev. B: Condens. Matter Mater. Phys.* **1999**, *59* (3), 1758−1775.

(33) Klimes, J.; Bowler, D. R.; Michaelides, A. Chemical accuracy for the van der Waals density functional. *J. Phys.: Condens. Matter* **2010**, *22* (2), 022201.

(34) Anisimov, V. I.; Zaanen, J.; Andersen, O. K. Band Theory and Mott Insulators - Hubbard-U Instead of Stoner-I. *Phys. Rev. B: Condens. Matter Mater. Phys.* **1991**, *44* (3), 943−954.

(35) Liu, L.; Ren, X.; Xie, J.; Cheng, B.; Liu, W.; An, T.; Qin, H.; Hu, J. Magnetic switches via electric field in BN nanoribbons. *Appl. Surf. Sci.* **2019**, *480*, 300−307.